Characterizing fracturing of clay-rich Lower Watrous rock: From laboratory experiments to nonlocal damage-based simulations

Nicolas Guy, Darius Seyedi, François Hild

Rock Mechanics and Rock Engineering manuscript No.
(will be inserted by the editor)

Characterizing fracturing of clay-rich Lower Watrous rock: From laboratory experiments to nonlocal damage-based simulations

N. Guy · D. M. Seyedi · F. Hild

Received: date / Accepted: date

Abstract The work presented herein aims at characterizing and modeling fracturing (*i.e.,* initiation and propagation of cracks) in a clay rich rock. The analysis is based on two experimental campaigns. The first one relies on a probabilistic analysis of crack initiation considering Brazilian and three-point flexural tests. The second one involves digital image correlation to characterize crack propagation. A nonlocal damage model based on stress regularization is used for the simulations. Two thresholds both based on regularized stress

N. Guy
BRGM, Natural Risks and CO_2 Storage Safety Division, 3 avenue Claude Guillemin, BP36009, 45060 Orléans, France
Present address: IFP Energies nouvelles, 1 & 4 avenue Bois-Préau, 92852 Rueil-Malmaison Cedex, France
Fax: +33-1-42576000
E-mail: nicolas.guy@ifpen.fr

D. M. Seyedi
BRGM, Natural Risks and CO_2 Storage Safety Division, 3 avenue Claude Guillemin, BP36009, 45060 Orléans, France
Present address: Andra, R & D Division, 1 rue Jean Monnet, 92290 Chatenay-Malabry, France

F. Hild
LMT, ENS Paris-Saclay / CNRS / Université Paris-Saclay, 61 avenue du Président Wilson, 94235 Cachan Cedex, France

fields are considered. They are determined from the experimental campaigns performed on Lower Watrous rock. The results obtained with the proposed approach are favorably compared with the experimental results.

Keywords Crack network · Fracture Toughness · Nonlocal damage · Rock Fracturing · Weibull model

List of symbols

$\boldsymbol{\sigma}$	Stress tensor
$\overline{\boldsymbol{\sigma}}$	Regularized stress tensor
ℓ_c	Characteristic length
Δ	Laplacian operator
$\boldsymbol{n}$	Normal to surface
P_i	Crack initiation probability
S_i	Crack initiation stress
$\frac{\sigma_0^m}{\lambda_0}$	Scale parameter
V_{el}	Volume of an element
m	Weibull modulus
σ_{ℓ_c}	nominal stress
S_g	Crack growth stress
K_c	Fracture toughness
Γ	Gamma function
ρ	Mass density
d	Damage
ψ_e	State potential
$\mathcal{C}$	Hooke's tensor
$\boldsymbol{\epsilon}$	Infinitesimal strain tensor
Y	Thermodynamic force associated with damage
H_e	Heaviside function
$\overline{\sigma}_I$	Maximum principal regularized stress
a	Half length of critical defect
σ_w	Weibull stress
σ_{wi}	Weibull stress associated with sample i
P_F	Failure probability
P_{Fi}	Failure probability associated with sample i
σ_f	Critical maximum principal stress

H	Stress heterogeneity factor
V	Sample volume
H_{br}	Stress heterogeneity factor for Brazilian test
V_{br}	Sample volume for Brazilian test
H_{fl}	Stress heterogeneity factor for three point flexural test
V_{fl}	Sample volume for three point flexural test
n_s	Total number of samples
R	Radius of Brazilian test sample
L	Length of Brazilian test sample
K_I	Mode I stress intensity factor
K_{II}	Mode II stress intensity factor
r_K	Ratio between mode II and mode I stress intensity factors

1 Introduction

The characterization and modeling of damage and cracking in quasi-brittle materials such as concrete and rocks is of great interest in different engineering applications such as deep geothermal energy production, CO_2 geological storage, nuclear waste underground disposal or for unconventional oil and gas production. Such applications require an accurate description of fracturing of geological formations to characterize structure stability and rock strength (Funatsu *et al.*, 2004). Furthermore characterizing rock fracturing can also be a key issue to evaluate induced changes in flow properties (Baghbanan and Lanru, 2007; Jobmann *et al.*, 2010) such as permeability and fracturing-induced leakage or pressure modification.

Damage, cracking and rock fracturing are based on two key phenomena, namely, crack initiation and propagation. The description of crack propagation in quasi-brittle materials remains a challenging task despite important efforts carried during past decades. In numerical simulations with standard (*i.e.,* local) softening damage models the strain field localizes in a band with a thickness of one element (Pietruszczak, 1981). The results exhibit a pathological dependence on the spatial discretization, namely, the mesh fineness and the orientation of elements. As an extreme case, it can be shown that for a very fine discretization the predicted fracture energy approaches zero (Pietruszczak, 1981; Bažant and Belytschko, 1985), which is unrealistic from a physical point of view. The loss of ellipticity of the equations describing the mechanical problem has been identified as the corresponding mathematical issue (Triantafyllidis and Aifantis, 1986; Lasry and Belytschko, 1988; De Borst *et al.*, 1993). Different regularization schemes have been proposed to avoid the ill-posedness of the mathematical description at a certain level of accumulated damage. Nonlocal damage models (Pijaudier-Cabot and Bažant, 1987; Bažant and Pijaudier-Cabot, 1988) provide a suitable framework to have mesh objective results when dealing with the post-localized behavior. Higher-order strain (Peerlings *et al.*, 1998; Lorentz and Benallal, 2005), stress (Guy, 2010;

Guy *et al.*, 2012) or damage (Lyakhovsky *et al.*, 2011) gradients are used to include a nonlocal effect and thus removing the sensitivity of the model to spatial discretization.

Moreover, geomaterials commonly exhibit large scatter on their mechanical parameters because of their natural components. Regarding clay-rich rocks, this heterogeneity may come from the variability of the mineral composition of the rock, *e.g.,* the clay content or the presence of flaws. Crack initiation in rocks usually has a random character with a scatter in initiation stress. The effect of this randomness on the cracking probability needs to be taken into account in both material behavior characterization and modeling (Guy *et al.*, 2010). This heterogeneity can be evaluated experimentally considering a relevant number of specimens, performing systematic failure tests and using an appropriate approach to analyze the results such as the methods proposed by Weibull (1939), and completed by the work of Beremin (1983) and Da Silva *et al.* (2004). Furthermore, the experimental identification of parameters describing crack propagation in quasi-brittle and heterogeneous material leads to specific challenges because of their brittleness. Several specific experimental procedures have been developed (Zuo *et al.*, 2014) such as Straight Edge Cracked Round Bar Bend (SECRBB (Bush, 1976)), or Chevron Bend (CB (Ouchterlony, 1988)) tests. Another test allowing a rock specimen to be pre-cracked without leading to brittle failure is the so-called Sandwiched-Beam (SB (Pancheri *et al.*, 1998)) test. With this method, crack propagation is controlled and therefore quantified before encountering specimen failure.

A complete study of rock fracturing from laboratory test to numerical modeling is presented in this paper. It is based on original experimental results and new validations of the numerical model introduced by the present authors. The latter is a nonlocal damage model using two thresholds based on a regularized stress field (Guy *et al.*, 2012). Each threshold is associated with a cracking regime. Crack initiation is characterized through a probabilistic analysis based on three-point flexural and Brazilian tests. Crack propagation is analyzed through SB tests with digital image correlation (Roux and Hild,

2006). In order to evaluate the relevance of the results obtained with the numerical model, the tests are simulated using the identified parameters.

2 Probabilistic nonlocal model for rock fracturing

The heterogeneity in rocks is always at the origin of the scatter observed in the measured failure stress of samples (Baecher and Einstein, 1981). The rock mass heterogeneity will be described by the presence of defects with a random distribution. The scatter of failure stress for rocks is explained by the presence of microcracks (*i.e.,* initial defects) that are at the origin of crack initiation, causing its subsequent failure. A probabilistic model based on a Poisson point process is used to describe this random character by relating the material microstructure and its macroscopic behavior. In the present work a probabilistic nonlocal model (Guy, 2010; Guy *et al.*, 2012) is used to study possible cracking of the rock mass due to stress changes. Two different thresholds are considered for crack initiation and propagation. A damage threshold based on the Weibull (1939) model is used to account for the stochastic nature of crack initiation(s) and then a fracture-mechanics-based threshold to model crack propagation. Both thresholds are probed by using a regularized stress field to avoid mesh dependence and localization phenomena. The regularization operation is performed over a characteristic length ℓ_c that must be long enough with respect to the size of the elements in the zone of interest. In the present case, it is proposed to choose the characteristic length equal to the largest defect size. This choice provides a crack initiation threshold greater than or equal to the crack growth threshold. The characteristic length stands thus for a micro-structural parameter that is the size of the largest initial crack modeled as a defect. The bigger cracks can be modeled as a set of completely damaged elements. The regularization operator reads

$$\overline{\boldsymbol{\sigma}} - \ell_c^2 \Delta \overline{\boldsymbol{\sigma}} = \boldsymbol{\sigma}, \;\; (\boldsymbol{\nabla}\, \overline{\boldsymbol{\sigma}}) \cdot \boldsymbol{n} = \mathbf{0} \tag{1}$$

where $\overline{\boldsymbol{\sigma}}$ is the regularized stress tensor and $\boldsymbol{\sigma}$ the Cauchy stress tensor. The vector $\boldsymbol{n}$ is normal to a surface where natural boundary conditions are considered. The used procedure is similar to the implicit gradient enhanced scheme proposed by Peerlings *et al.* (1998, 2001).

Let us consider the case of crack initiation under tensile stresses, *i.e.,* in mode I. In this setting, the initiation of new macrocracks follows the weakest link assumption and a Weibull model can explain the scatter of the experimental results. An initiation probability $P_i\left(el\right) \in [0;1]$ calculated from a uniform distribution is assigned to each sub-domain (*i.e.,* each element). An initiation stress is then calculated for each sub-domain from an inverse Weibull law

$$S_i\left(el\right) = \frac{\sigma_0}{\left(\lambda_0 V_{el}\right)^{\frac{1}{m}}} \left[-\ln\left(1 - P_i\left(el\right)\right)\right]^{\frac{1}{m}} \tag{2}$$

where V_{el} is the volume of the considered element, m the Weibull modulus, and $\frac{\sigma_0^m}{\lambda_0}$ the scale parameter. A crack will initiate in the considered element if the regularized maximum principal stress reaches $S_i\left(el\right)$. The initiated macrocracks are assumed to be perpendicular to the regularized maximum principal stress direction. For a given characteristic length, a nominal stress is defined as

$$\sigma_{\ell_c} = \sigma_0 / \left(\lambda_0 \ell_c^3\right)^{1/m} \tag{3}$$

which is useful to obtain an estimation of the stress state associated with crack initiation. It corresponds to the necessary loading leading to initiate a crack in a loaded element of volume ℓ_c^3 with a probability of $1-1/e \approx 0.63$. Considering the two-dimensional case of a crack in an elastic medium submitted to a far field loading, the asymptotic Westergaard solution (Kanninen *et al.*, 1982) gives a good approximation of the stress field around the crack tip. Considering Equation (1) as a nonhomogeneous Helmholtz equation, the proposed operator provides a regularized stress field in the vicinity of the crack tip corresponding to Westergaard asymptotic solution. The present procedure allows the stress intensity factor to be calculated without any mesh refinement for a propagating crack. Therefore, a direct transition from a damage-mechanics-based model for crack initiation to a fracture-mechanics-based model for crack propagation is

provided. In addition, both models use the same variable, *i.e.,* the regularized stress. In this framework the crack propagation threshold reads

$$S_g\left(el\right) = \frac{6\Gamma^2\left(\frac{3}{4}\right)}{5\pi}\frac{K_c}{\sqrt{\pi\ell_c}} \tag{4}$$

where K_c is the fracture toughness of the rock and Γ the Gamma function. For a mode I crack, the above-mentioned criterion tends to a fracture mechanics threshold for an open crack when the characteristic length ℓ_c becomes small compared with the macroscopic scale. It is to be noted that the introduced criterion accounts for mixed mode propagation

$$K_c \leq \frac{5K_I + \sqrt{K_I^2 + 16K_{II}^2}}{6} \approx K_I + \frac{2}{3}K_{II} \tag{5}$$

where K_I and K_{II} stand for the mode I and II stress intensity factors respectively. A perfectly brittle behavior of an isotropic material is considered as a local damage law. The Helmholtz state potential thus reads

$$\rho\psi_e = \frac{1}{2}\left(1-d\right)\ \boldsymbol{\epsilon}\ \mathcal{C}\ \boldsymbol{\epsilon} \tag{6}$$

where $\mathcal{C}$ is Hooke's tensor of the virgin material, ρ the mass density, $\boldsymbol{\epsilon}$ the infinitesimal strain tensor, and d the damage variable. From the state potential, the stress-strain relation is obtained

$$\sigma = \rho\frac{\partial\psi_e}{\partial\boldsymbol{\epsilon}} = \left(1-d\right)\mathcal{C}\ \boldsymbol{\epsilon}. \tag{7}$$

In this framework the medium is considered as having a linear elastic behavior, which is a simplifying assumption as viscosity may influence both long-term relaxation and short term dissipation, thereby stabilizing dissipation and damage growth especially for unstable crack propagation (Lyakhovsky *et al.*, 2011). These effects are not considered herein for the sake of simplicity since the study focuses on stable crack propagation under mechanical loadings that do not involve significant strain due to long-term relaxation. The thermodynamic force associated with the damage variable d is defined as

$$Y = -\rho\frac{\partial\psi_e}{\partial d} = \frac{1}{2}\boldsymbol{\epsilon}\ \mathcal{C}\ \boldsymbol{\epsilon}. \tag{8}$$

Damage growth is written as

$$d = H_e\left(\langle \overline{\sigma}_I - S_i \rangle + \langle \overline{\sigma}_I - S_g \rangle\right) \quad \text{when} \quad \dot{d} \geq 0 \tag{9}$$

where H_e denotes the Heaviside step function, $\overline{\sigma}_I$ the maximum principal regularized stress, S_i and S_g the initiation and propagation thresholds.

The crack initiation criterion is introduced considering that a crack initiation stress is associated with each initial defect. The initial defects greater than $2\ell_c$ cannot be considered in this way. Let us consider a domain with a critical defect of half-length a. Assuming that the characteristic length is greater than a leads to

$$S_i = \frac{K_c}{\sqrt{\pi a}} \geq \frac{K_c}{\sqrt{\pi \ell_c}} > \frac{6\Gamma\left(\frac{3}{4}\right)}{5\pi} \frac{K_c}{\sqrt{\pi \ell_c}} = S_g. \tag{10}$$

A characteristic length greater than the size of the largest initial defect provides a crack initiation threshold greater than the propagation threshold. The characteristic length corresponds to a microstructural parameter that is the size of the largest initial crack modeled as a defect. Initial cracks of size larger than $2\ell_c$ can be modeled as a set of completely damaged elements.

3 Characterization of rock fracturing

In this section, the consistency of both experimental and numerical results provided by the model presented in Section 2 is checked. The initiation threshold is studied first through Brazilian test simulation. In order to validate the crack propagation threshold, crack propagation in a numerical sample is simulated with boundary conditions corresponding to a Sandwiched-Beam test. In each simulation, the characteristics used to describe the studied rock are issued from an experimental campaign.

The study is performed on rock samples from the Weyburn site (Canada). The latter is considered as a demonstration site for CO_2 storage (Preston *et al.*, 2005). The International Energy Agency Green House Gas (IEAGHG) Weyburn-Midale CO_2 storage and monitoring project was designed to assess the technical feasibility of CO_2 geological storage at large scale. The Weyburn

and Midale oil fields are located near Midale in Saskatchewan state. Various Enhanced Oil Recovery (EOR) techniques were used before the introduction of CO_2 for EOR in 2000. The rock samples were extracted from a depth of 1,300 m. They are located in a particular geological layer called Lower Watrous. Lower Watrous is considered as a potential caprock for CO_2 storage in the Weyburn site.

The studied rock has a complex lithology. It is a clay-rich rock with embedded grains that are mostly made of the lutites size (*i.e.,* a diameter less than 62.5 μm (Le Nindre and Gauss, 2004)). The samples have a diameter of 86 mm for a length of 2.0 to 2.4 times their diameter (Figure 1). Even if the studied rock has a fine microstructure, it contains mineral inclusions (made of quartz). Their diameter can reach few tenths of millimeters (Figure 1).

The microstructure is shown in Figure 2. It is made of clastic and granitic grains embedded in a clay-dolomitic matrix as shown in Figure 2(a). The samples also contain quartz inclusions at a higher scale, a part of an inclusion is shown in Figure 2(b). Two different scales can thus be distinguished, namely, the scale of the clay matrix and that of quartz inclusions, which provide a heterogeneity at a larger scale. The material has a random porosity. The average volume fraction is 4 % (Le Nindre and Gauss, 2004).

The Young's modulus and Poisson's ratio are identified via compressive tests shown in Figure 3(a). The blue lines in sub-Figures 3(b-c) represent the changes of axial and radial strains measured using strain gauges under an evolving axial stress respectively. The slope of the black line in Figure 3(b) is used to calculate the Young's modulus and the slope of the black line in Figure 3(c) is used to evaluate the Poisson's ratio. The identified Young's modulus is equal to 16 GPa and the Poisson's ratio is equal to 0.15. As it can be seen in Figure 3(b), it can be considered that the studied rock, as other geomaterials, exhibits a brittle behavior under unconfined compressive loading.

3.1 Crack initiation

In this section, the behavior of the studied rock in terms of crack initiation in mode I is first characterized considering a Weibull model. A two-parameter Weibull model is selected to describe the behavior of the rock samples at failure. The Weibull parameters are determined using three-point flexural and Brazilian tests, thereby providing two different scales of effective volumes. Then, the ability of the numerical model to properly describe crack initiation is studied by modeling Brazilian tests.

3.1.1 Identification of Weibull parameters

The Weibull parameters are identified through an experimental campaign based on three-point flexural and Brazilian tests. The identification method (Da Silva *et al.*, 2004) is such that it allows results issued from the two types of tests to be considered at the same time. Thirty three-point flexural tests and 34 Brazilian tests were performed. For the three-point flexural tests the samples dimensions are $h \approx 18.75$ mm, $b \approx 18.75$ mm and $L = 75.0$ mm. For the Brazilian tests, the sample radius is $R \approx 43$ mm and its length is $L \approx 80$ mm. For each broken sample, a maximum principal stress σ_f is calculated from the actual sample dimensions and load to failure. In order to identify only one set of Weibull parameters that suits both series of tests, a Weibull stress (Beremin, 1983; Da Silva *et al.*, 2004) is introduced for each broken sample

$$\sigma_w = \sigma_f \left(HV\lambda_0\right)^{\frac{1}{m}} \tag{11}$$

where H is the stress heterogeneity factor, and V the sample volume that are equal to H_{br} and V_{br} for the Brazilian tests and to H_{fl} and V_{fl} for the three-point flexural tests. Therefore, the Weibull parameters, m the Weibull modulus and σ_0^m/λ_0 the scale parameter, can be deduced from the Weibull stresses in ascending order σ_{wi}. The linear regression method can be used to identify the parameters as it is relevant when few experimental data are available (Gosh, 1999; Wu *et al.*, 2006). The principle is to assign to each Weibull stress σ_{wi} a

failure probability P_{Fi} such that

$$P_{Fi} = \frac{i}{n_s + 1} \tag{12}$$

where n_s is the total number of samples. It can be deduce from the Weibull model that

$$\ln\left[-\ln\left(1 - P_{Fi}\right)\right] = m\ \left[\ln(\sigma_{wi}) - \ln\left(\sigma_0\right)\right], \tag{13}$$

therefore the Weibull parameters can be deduced from an iterative least squares analysis (Da Silva *et al.*, 2004). The Weibull diagram is shown in Figure 4. The identified Weibull modulus is $m = 6.0$, which corresponds to a clearly heterogeneous material; it is in the typical range of values for rocks (*i.e.,* $3 \leq m \leq 9$). As it can be seen in Figure 4, there is a good agreement between experimental data and the model.

It is to be noted that the use of a two-parameter Weibull model leads to a conservative estimation of failure probability for the lowest stresses as no threshold is considered.

3.1.2 Validation of initiation modeling

In order to validate the initiation threshold, numerical modeling of Brazilian tests is performed. The rock samples are modeled in a 2D setting under plane strain hypothesis by disks that have a radius of $R = 43$ mm. The rock parameters are those identified previously. For the computation of the initiation threshold the element volume is required. In the present case the length of the specimens $L = 85$ mm is considered as the thickness of the element. The Weibull modulus is $m = 6.0$ and the scale parameter is $\sigma_0^m/\lambda_0 = 7.3 \times 10^{35}$ Pa^{m}m^3. The characteristic length is considered as $\ell_c = 2$ mm to be small enough to allow for a relevant description of the stress state in the numerical specimen with the regularized stress. A characteristic length of $\ell_c = 2$ mm implies that initial cracks (*i.e.,* initial defects) are smaller than 4 mm, which is a reasonable hypothesis. The nominal initiation stress is $\sigma_{\ell_c} = \sigma_0 / \left(\lambda_0 \ell_c^3\right)^{1/m} = 21.2$ MPa. The numerical model is shown in Figure 5.

The displacements are zero on the bottom of the structure. For the highest point, the horizontal displacements are zero and a vertical force is applied. The mesh is shown in Figure 5(a). In Figure 5(b) the initiation thresholds obtained for each element of one numerical sample are mapped. The initiation threshold for each element is obtained considering its size and following a random selection of an initiation probability from a uniform distribution using Equation (2). This procedure results in a scattered map ranging from 3.6 MPa to 40 MPa. Only the lowest initiation thresholds have an influence on the results as the potential initiation sites. In the simulations performed with Code_Aster (2017), the regularized stress field tends to lead to crack initiation in the middle of the specimen, which is consistent with experimental observations.

The theoretical failure probability reads

$$P_F = 1 - \exp\left[-\left(\frac{\sigma_w}{\sigma_0}\right)^m\right]. \tag{14}$$

One hundred simulations were performed to obtain one hundred Weibull stresses σ_{wi}. For each Weibull stress i a failure probability is defined $P_{Fi} = i/(n+1)$. The results of numerical simulations, analytical model (Equation (14)) and experiments are plotted in Figure 6.

The results provided by the three approaches are consistent. Only small differences are observed for low probabilities. This difference is due to the cut-off of the lowest part of the Weibull distribution associated with initial defects due to the consistency condition (Equation (10)). In the present case, the consistency condition leads to the hypothesis that initial cracks are smaller than 4 mm. It appears that for low probabilities the numerical model is closer to the experimental results than the analytical model.

3.2 Crack propagation

The toughness describes the material ability to resist to crack propagation. In linear elastic fracture mechanics, the fracture toughness is usually compared

to stress intensity factors to predict crack propagation. The material toughness can be identified from three-point flexural tests performed on notched specimens even if in this context crack propagation is unstable for brittle materials. An analytical solution can be used to link the failure load with the material toughness and the notch length (Murakami, 1987). Pre-cracking can be performed with Sandwiched-Beam tests that allow for stable crack propagation (Srawley, 1976; Nose and Fuji, 1988; Lawn, 1993). Digital image correlation (DIC) (Sutton *et al.*, 2009; Hild and Roux, 2006) is an experimental method that allows displacement fields to be measured and that can be used for detecting and quantifying crack initiation and propagation (Roux and Hild, 2006). Specific DIC features have been developed in order to calculate stress intensity factors (Forquin *et al.*, 2004; Roux and Hild, 2006). They will be used hereafter. The material toughness is measured with a two-step experimental campaign consisting of first pre-cracking the sample (here with an SB configuration) and then loading the pre-cracked sample in three-point flexure up to failure.

3.2.1 Image-based identification of fracture toughness

The failure of a brittle material tends to be very sudden because it commonly results from unstable crack propagation. Several methods exist to perform sample pre-cracking (Nose and Fuji, 1988; Lawn, 1993). One solution is to load the specimen in such a way that crack initiation and stable propagation are possible (*e.g.,* Sandwiched-Beam (SB) test (Pancheri *et al.*, 1998)). The SB test uses three beams, namely, the central beam to be pre-cracked and two other identical beams made of a more rigid material as shown in Figure 7.

In the present study, the lower and upper beams are made of aluminium alloy and have a Young's modulus of 70 GPa. Each beam has a thickness of 18.75 mm, the central beam has a height of 18.75 mm and the lower and upper ones a height of 20.00 mm. All the beams have a length of more than 75.0 mm. Crack initiation and location can be detected with the use of DIC

(Figure 8). In the present case, a global DIC code with Q4 quadrilaterals is utilized (Besnard *et al.*, 2006). From the measured displacement field, the mean infinitesimal strains per element are computed. The maximum eigen strain field exhibits a very localized region corresponding to the presence of a crack.

At this stage of the experimental process, the material arrest toughness can be deduced from the observed displacement fields (Roux and Hild, 2006) under the assumption that the crack is propagating. After sample pre-cracking, three-point flexural tests are performed for toughness identification with the use of DIC. Figure 9 shows the results for sample no. 2 in three-point flexure for an applied load of $F = 350$ N. The horizontal displacement field is shown after rigid body translation removal. The crack tip location used for the post-processing step is plotted in white. The area in black is used for the post-processing based on a comparison between identified displacement field and Williams' series of the displacement field close to the singularity (Roux and Hild, 2006).

The stress intensity factor is estimated for different loading levels in order to obtain a better estimation of the fracture toughness as shown in Figure 10. Knowing the failure load $F_c = 368$ N for the considered sample, the fracture toughness is estimated by linearly extrapolating the stress intensity factor with the applied load. For the present test a fracture toughness of 1.04 MPa$\sqrt{\text{m}}$ is obtained.

Five samples (no. 1 to 5) have led to fracture toughness identification for both steps of the experimental campaign. The results are summarized in Table 1. It is worth noting that the residual error in terms of displacement given for the identification corresponding to the maximum load is low compared with the displacement uncertainty levels (*i.e.,* 0.02 pixel). Therefore, the estimated stress intensity factors are deemed trustworthy. The mode I stress intensity factors are scattered from $K_I(\text{a}) = 0.11$ MPa$\sqrt{\text{m}}$ to $K_I(\text{a}) = 0.32$ MPa$\sqrt{\text{m}}$ for the pre-cracking phase, and between $K_I(\text{b}) = 0.16$ MPa$\sqrt{\text{m}}$ and $K_I(\text{b}) =$

1.04 MPa$\sqrt{\text{m}}$ for the subsequent three-point flexural tests. The observed scatter again reflects the material heterogeneity.

Despite scattered results, two clear tendencies can be pointed out. First, the mode II stress intensity factors are significantly lower than mode I levels. The mode II stress intensity factors are relatively higher for the SB tests as shown by the values $r_K = K_{II}/K_I$. It means that the cracking mode is mode I dominant for the three-point flexural tests. This result can be explained by the confinement induced by the use of the metallic beams. Second, the stress intensity factors estimated for both tests are different with averages of $K_I(\text{a}) = 0.21$ MPa$\sqrt{\text{m}}$ and $K_I(\text{b}) = 0.55$ MPa$\sqrt{\text{m}}$. This tendency (of finding lower values for the pre-cracking tests) is observed for each sample. It can be explained by the fact that the stress intensity factors identified in three-point flexural tests are associated with crack propagation inception whereas those determined with SB (pre-cracking) tests correspond to crack arrest. Given the experimental scatter, it is chosen to select a single value $K_c = 0.21$ MPa$\sqrt{\text{m}}$ as a conservative estimate.

3.2.2 Validation of crack propagation modeling

In order to validate the crack propagation threshold introduced in Section 2, the results obtained with DIC are compared with those issued from numerical simulations. First, an SB test is modeled. The DIC results are based on a spatial discretization of 8×8 pixel elements (1 pixel ≈ 20.7 μm). The measured displacements on the external boundary of the analyzed area are used as (Dirichlet) boundary conditions of the numerical model. In the present case, the external boundary is a rectangle and the finite element models used in the numerical computations are based on the same mesh used for DIC purposes. With such setting there is no need to model friction between the different beams of the SB test, and realistic boundary conditions are prescribed as measured via DIC. The crack initiation threshold is uniform and considered high enough in the modeled domain, $S_i = 10$ MPa to ensure that crack initiation

appears at the right location, which is induced by the displacement loading on the bottom face. The high horizontal displacement gradient due to the initiated crack leads to a loading that induces a very significant local increase of the regularized stress, thereby initiating the crack in the numerical model. To describe crack propagation a fracture toughness of $K_c = 0.21$ MPa$\sqrt{\text{m}}$ is considered (see above).

The horizontal displacement fields measured from an experiment and simulated are shown in Figure 11 together with the damage field at the end of the numerical computation. The results of the numerical computation are in good agreement with the experimental observations. In both cases the crack length is of the same order. A difference is observed concerning the crack orientation. For the numerical computation, the crack orientation has an angle of 3° with the vertical axis at initiation. After initiation, the crack propagation direction changes and tends to be inclined by 30°. For the experimental results, the crack orientation is of 7° for most of the propagation and tends to turn at the end of the experiments. This difference in terms of orientation is not surprising considering the applied load on the lower boundary. The displacement field used as a boundary condition in the computation does not only exhibit a significant gradient at the crack base for the horizontal value but also for the vertical one leading to a mode II loading of the crack in the 2D simulation. Therefore it is relevant that the crack tends to be inclined in the simulation.

A major difference between the experiment and the simulation is that the experiment is performed on a 3D sample and that the crack propagation during the experiment is indeed related to a 3D displacement field. The displacement estimated through DIC at the surface could be only partially representative of the 3D displacement field. Therefore, the observed gradient of vertical displacement at the crack base could only concern the vicinity of the surface of the observed specimen, leading to a less inclined crack in the experiment than in the simulation. Moreover, Lower Watrous presents a slight elastic anisotropy as most sedimentary rocks. This stiffness anisotropy may also affect the crack propagation orientation.

4 Conclusions

The fracturing of clay-rich rock samples has been studied in both experimental and numerical ways. The samples have been extracted from the Weyburn site (Canada). An extensive experimental campaign enabled for the identification of elastic parameters thanks to uniaxial compression tests. Weibull parameters were determined via Brazilian and three-point flexural tests. The Weibull parameters allow crack initiation to be described in a probabilistic framework. Sandwiched-beam and single edge cracked beam tests enabled the toughness at crack arrest and propagation inception to be studied thanks to digital image correlation. The toughness is the key property to analyze crack propagation. Such data are quite unique for such type of rocks.

The capacities of a probabilistic non-local damage model to describe crack initiation and propagation are analyzed through the comparison of experimental and numerical results. Each of these mechanisms has been associated with an experimental process. Numerical simulations of Brazilian tests are performed in order to evaluate the numerical model ability to reproduce crack initiation. A consistent description of the tests with a Weibull law shows that initiation is dominant in such situations (*i.e.,* the weakest link hypothesis is satisfied). Simulation of crack propagation in a numerical model loaded with boundary displacements issued from digital image correlation measurements are also performed and yields consistent results in comparison with experiments. The crack length estimation is relevant and the crack orientation estimation is slightly different from the experiment.

To enhance the results, an extensive study of the effect of mixed-mode loading and especially on the effect of mode II loading could be interesting. Further, no scatter in terms of fracture toughness was considered. This may also change the actual path of the crack. Yet, it appears that the numerical model is able to provide a good prediction of crack propagation and especially of its length. However, differences in terms of crack orientation between experiments and simulations are observed. This could be explained by 3D effects

that are not considered in the 2D simulations, and elastic anisotropy of the studied rock.

Acknowledgements This work was funded by BRGM through an "Institut Carnot" research grant. The authors wish to thank Dr. Steve Whittaker and Saskatchewan Industry and Resource for kindly providing the samples of Lower Watrous caprock.

References

Baecher GB, Einstein HH (1981) Scale effect in rock testing. Geophys Res Let 8:671-674.

Baghbanan A, Lanru J (2007) Hydraulic properties of fractured masses with correlated fracture length and aperture. Int J R Mech Min Sci 44:704-719.

Bažant Z, Belytschko TB (1985) Wave propagation in strain-softening bar: exact solution. J Eng Mech 111:381-389.

Bažant ZP, Pijaudier-Cabot G (1988) Nonlocal continuum damage, localization instability and convergence. J Appl Mech 55:521-539.

Beremin FM (1983) A local criterion for cleavage fracture of a nuclear pressure vessel steel. Metall Trans 14:2277-2287.

Besnard G, Hild F, Roux S (2006) "Finite-element" displacement fields analysis from digital images: Application to Portevin-Le Chatelier bands. Exp Mech 46:789-804.

Bush AJ (1976) Experimentally determined stress-intensity factors for single-edge-crack round bars in bending. Exp Mech 16:249-257.

Code_Aster (2017) *http://www.code-aster.org.* EDF R&D.

Da Silva ACR, Proença SPB, Billardon R, Hild F (2004) Probabilistic approach to predict cracking in lightly reinforced microconcrete panels. J Eng Mech 130:931-941.

De Borst R, Sluys LJ, Muhlaus HB, Pamin J (1993) Fundamental issues in finite element analysis of localization of deformation. Eng Comp 10:99-121.

Forquin P, Rota L, Charles Y, Hild F (2004) A method to determine the macroscopic toughness scatter of brittle materials. Eur J Mech - A/ Sol 125:171-187.

Funatsu T, Seto M, Shimada H, Matsui K, Kuruppu M (2004) Combined effects of increasing temperature and confining pressure on the fracture toughness of clay bearing rocks. Int J R Mech Min Sci 41:927-938.

Gosh A (1999) A FORTRAN program for fitting Weibull distribution and generating samples. Comp & Geosc 25:729-738.

Guy N (2010) Modélisation probabiliste de l'endommagement des roches : application au stockage géologique du CO_2. PhD thesis, Ecole Normale Supérieure de Cachan.

Guy N, Seyedi D, Hild F (2010) Hydro-mechanical modelling of geological CO2 storage and the study of possible caprock fracture mechanisms. Georisk 4:110-117.

Guy N, Seyedi D, Hild F (2012) A probabilistic nonlocal model for crack initiation and propagation in heterogeneous brittle materials. Int J Num Meth Eng 90:1053-1072.

Hild F, Roux S (2006) Digital image correlation: from displacement measurement to identification of elastic properties - a review. Strain 42:69-80.

Jobmann M, Wilsnack T, Voigt HD (2010) Investigation of damage induced permeability of Opalinus clay. Int J R Mech Min Sci 47:279-285.

Kanninen MF, Brust FW, Ahmad J, Abou-Sayed IS (1982) The numerical simulation of crack growth in weld-induced residual stress fields. In Residual stress and stress relaxation, (ed. E. Kula and V. Weiss), Plenum Press, New York, pp 975-986.

Lasry D, Belytschko T (1988) Localization limiters in transient problems. Int J Sol Struct 24:581-597.

Lawn BR (1993) Fracture of brittle material. Cambridge University Press.

Le Nindre YM, Gauss I (2004) Characterisation of the lower watrous aquitard as major seal for CO_2 geological sequestration. 7^{th} International Conference on Greenhouse Gas Control Technologies, September 5-9, Vancouver, Canada.

Lorentz E, Benallal A (2005) Gradient constitutive relations: numerical aspects and application to gradient damage. Comput Meth Appl Mech Eng 194:5191-5220.

Lyakhovsky V, Hamiel Y, Ben-Zion Y (2011) A non-local visco-elastic damage model and dynamic fracturing. J. Mech. Phys. Solids 59:1752-1776.

Murakami Y (1987) Stress intensity factors handbook. Pergamon.

Nose T, Fuji T (1988) Evaluation of fracture toughness for ceramics materials by a Single-Edge-Precracked-Beam method. J Am Ceram Soc 71:328-333.

Ouchterlony F (1988) ISRM commission on testing methods; suggested methods for determining fracture toughness of rock. Int J R Mech Min Sci **25**:71-96.

Pancheri P, Bosetti P, Dal Maschio R, Sglavo VM (1998) Production of sharp cracks in ceramic materials by three-point bending of sandwiched specimens. Eng Frac Mech 59:447-456.

Peerlings RHJ, de Borst R, Brekelmans WAM, Geers MGD (1998) Gradient-enhanced damage modelling of concrete fracture. Mech Cohes-Frict Mater 3:323-342.

Peerlings RHJ, Geers MGD, de Borst R, Brekelmans WAM (2001) A critical comparison of non-local and gradient-enhanced softening continua. Int J Sol Struct 38:7723-7746.

Pietruszczak S, Mróz Z (1981) Finite Element Analysis of Deformation of Strain-softening Materials. Int J Num Meth Eng 17:327-334.

Pijaudier-Cabot G, Bažant ZP (1987) Nonlocal damage theory. J Eng Mech 113:1512-1533.

Preston C, Monea M, Jazrawi W, Brown K, Whittaker S, White D, Law D, Chalaturnyk R, Rostron B (2005) IEA GHG Weyburn CO_2 monitoring and storage project. Fuel Proces Tech 86:1547-1568.

Roux S, Hild F (2006) Stress intensity factor measurements from digital image correlation: post-processing and integrated approaches. Int J Fract 140:141-157.

Srawley JE (1976) Wide range stress intensity factor expressions for ASTM E399 standard fracture thoughness specimens. Int J Frac 12:475-476.

Sutton MA, Orteu JJ, Schreier H (2009) Image correlation for shape, motion and deformation measurements: Basic Concepts, Theory and Applications. Springer, New York, USA.

Triantafyllidis N, Aifantis EC (1986) A gradient approach to localization of deformation: I. Hyperelastic materials. J Elasticity 16:225-237.

Weibull W (1939) A Statistical theory of the strength of materials. Royal Swedish Institute for Engineering Research.

Wu D, Zhou J, Li Y (2006) Unbiased estimation of Weibull parameters with the linear regression method. J Eur Ceram Soc 26:1099-1105.

Zuo JP, He-Ping X, Feng D, Yang J (2014) Three point bending test investigation of the fracture behavior of siltstone after thermal treatment. Int J R Mech Min Sci 70:133-143.

Fig. 1 Caprock sample 86 mm in diameter for a length of 180 mm.

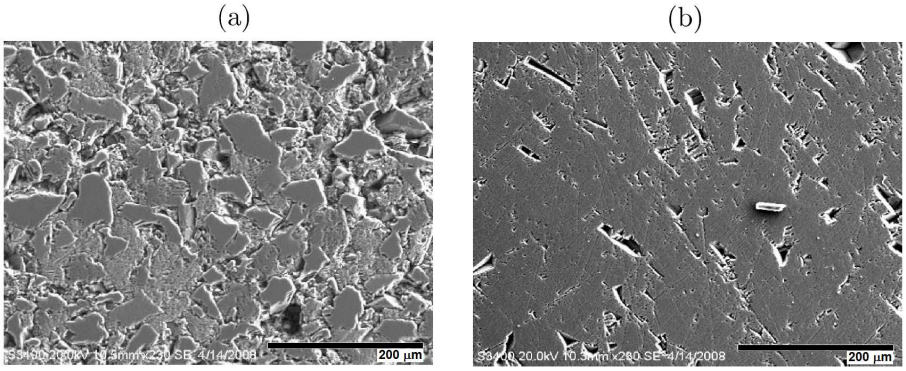

Fig. 2 (a) Grains in clay-dolomitic matrix. (b) Quartz mineral inclusion at the same scale.

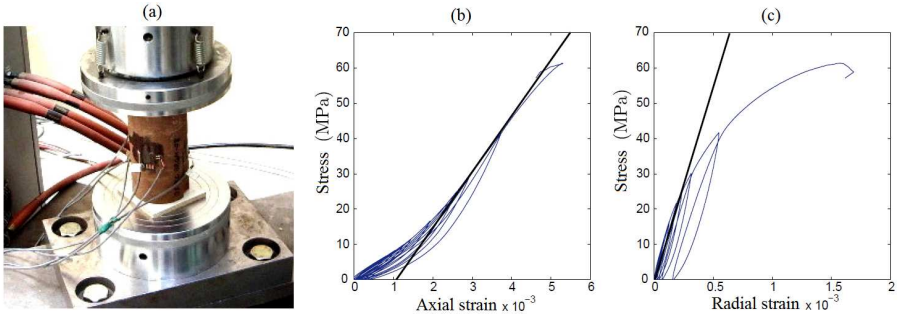

Fig. 3 (a) Compression test. Change of axial (b) and radial (c) strains measured using strain gauges under an evolving axial stress.

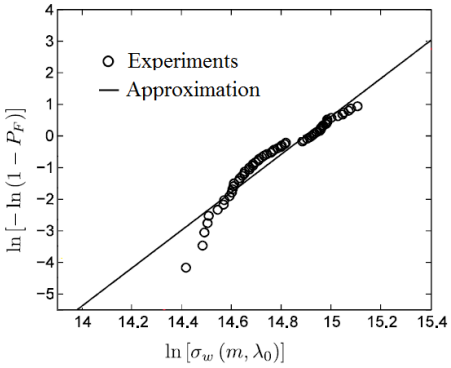

Fig. 4 Modified Weibull diagram for the identification of parameters based on three-point flexural and Brazilian tests.

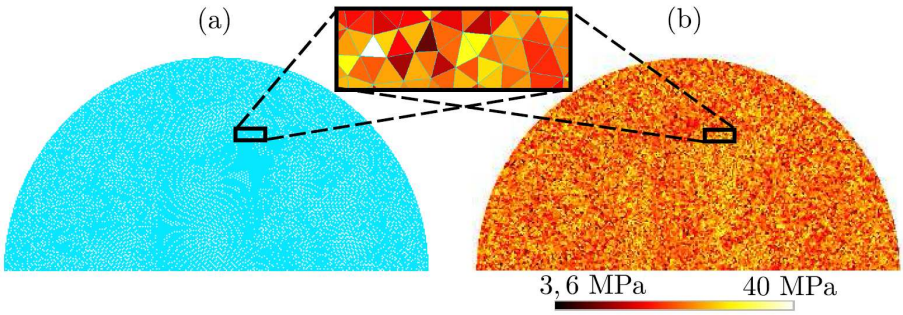

Fig. 5 Mesh (a) and crack initiation threshold (b) for the upper half of the model used to simulate Brazilian tests.

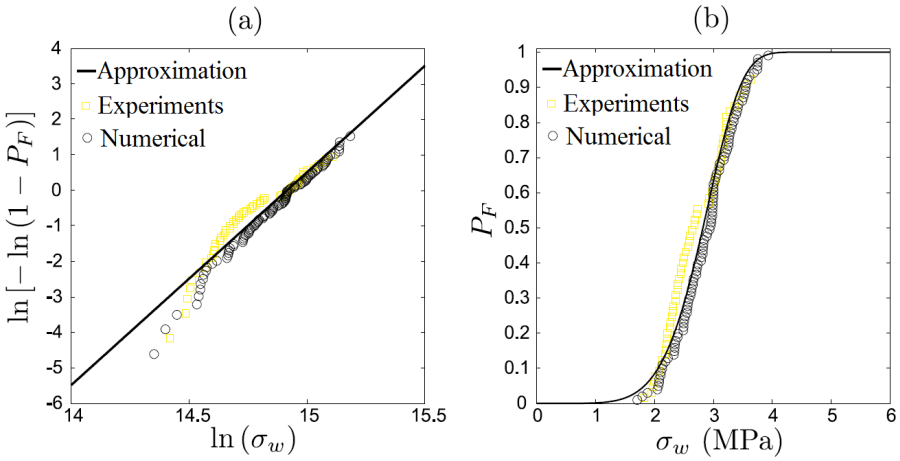

Fig. 6 Modified Weibull diagram (a) and failure probability P_F as functions of the Weibull stress σ_w (b) for the numerical, analytical and experimental approaches.

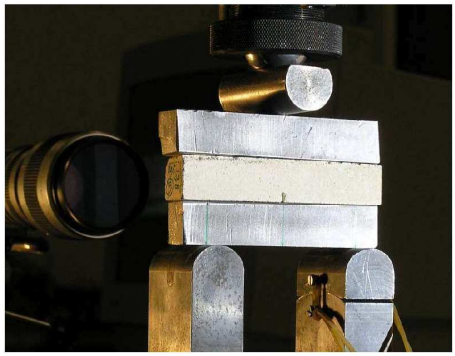

Fig. 7 Sandwiched-Beam test in which the rock sample is loaded with the two aluminum alloy beams.

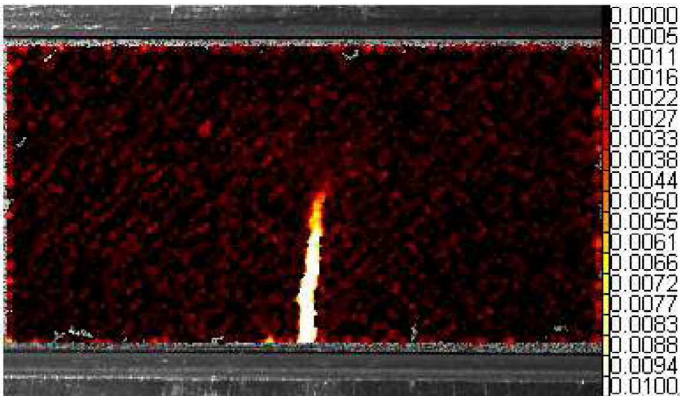

Fig. 8 Maximum eigen strain field in sample no. 2 when pre-cracked. The physical size of 1 pixel is $\approx$ 20.7 μm.

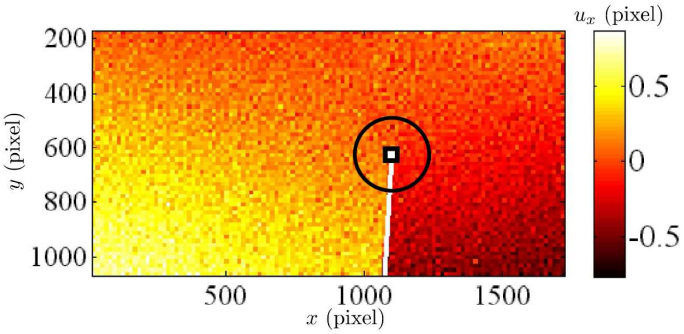

Fig. 9 Measured horizontal displacement field (expressed in pixels) when rigid body translations have been removed. Pre-cracked sample (no. 2) submitted to a load $F = 350$ N in three-point flexural test. The physical size of 1 pixel is $\approx$ 20.3 μm.

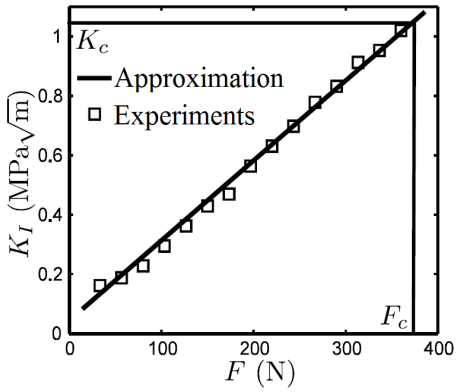

Fig. 10 Change of mode I stress intensity factor with applied load.

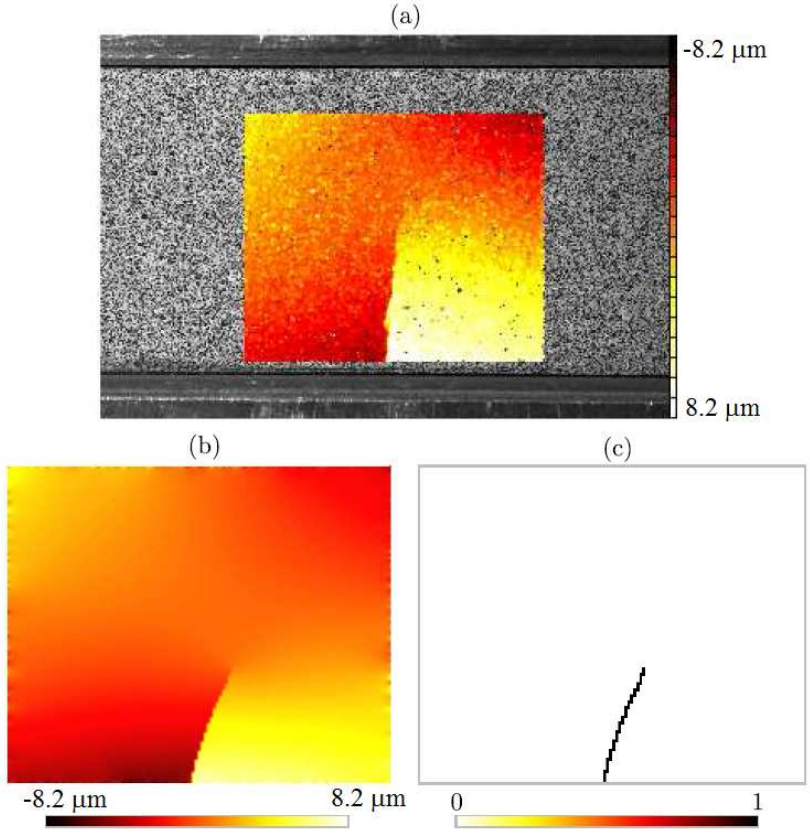

Fig. 11 (a) Horizontal measured displacement field. (b) Simulated displacement field. (c) Damage field for sample no. 2 in the Sandwiched-Beam test.

Table 1 Toughness results for Sandwiched-Beam tests (a) and three-point flexural tests (b) for the five studied samples.

Sample	1	2	3	4	5	average
K_I (MPa$\sqrt{\text{m}}$) (a)	0.13	0.31	0.11	0.32	0.19	0.21
K_{II} (MPa$\sqrt{\text{m}}$) (a)	0.07	0.12	0.05	0.20	0.11	0.11
$r_K = K_{II}/K_I$ (a)	0.54	0.39	0.45	0.62	0.58	0.52
Error (pixel) (a)	0.03	0.02	0.02	0.02	0.02	0.02
Resolution (μm/pixel) (a)	20.5	20.7	20.7	20.6	20.8	20.7
K_I (MPa$\sqrt{\text{m}}$) (b)	0.44	1.04	0.16	0.40	0.72	0.55
K_{II} (MPa$\sqrt{\text{m}}$) (b)	0.07	0.13	0.04	0.02	0.11	0.07
$r_K = K_{II}/K_I$ (b)	0.16	0.13	0.25	0.05	0.015	0.13
Error (pixel) (b)	0.02	0.09	0.02	0.02	0.04	0.04
Resolution (μm/pixel) (b)	20.1	20.3	20.3	20.6	20.4	20.3